Optically controlled dense current structures driven by relativistic plasma aperture-induced diffraction

B. Gonzalez-Izquierdo,[1] R. J. Gray,[1] M. King,[1] R. J. Dance,[1] R. Wilson,[1] J. McCreadie,[1] N. M. H. Butler,[1] R. Capdessus,[1] S. Hawkes,[2] J. S. Green,[2] M. Borghesi,[3] D. Neely,[2,1] and P. McKenna[1,*]

[1]*SUPA Department of Physics, University of Strathclyde, Glasgow G4 0NG, UK*

[2]*Central Laser Facility, STFC Rutherford Appleton Laboratory, Oxfordshire OX11 0QX, UK*

[3]*Centre for Plasma Physics, Queens University Belfast, Belfast BT7 1NN, UK*

Abstract

The collective response of charged particles to intense fields is intrinsic to plasma accelerators and radiation sources, relativistic optics and many astrophysical phenomena. Here we show that the fundamental optical process of diffraction occurs via the generation of a *relativistic plasma aperture* in thin foils undergoing relativistic induced transparency. The plasma electrons collectively respond to the resulting near-field diffraction pattern, producing a beam of energetic electrons with spatial structure which can be controlled by variation of the laser polarization, wavelength and focused intensity profile. The concept is demonstrated numerically and verified experimentally. The results provide new understanding of the formation of current structures in the relativistically transparent regime of laser-plasma interactions and is a viable step towards optical control of charged particle dynamics in laser-driven sources.

* Electronic address: paul.mckenna@strath.ac.uk

The formation of current structures due to the collective response of charged particles to a perturbation is one of the most fundamental properties of plasma. This is manifest in plasma dynamics ranging from flares and X-ray jets on the sun to disruptive instabilities in fusion plasmas. This feature is also exploited to great effect in the development of compact laser-based particle accelerators and radiation sources, which have wide-ranging potential applications in science, medicine and industry. Controlling the collective motion of plasma electrons in response to perturbation produced by intense laser light is key to the development of these novel sources. Pertinent examples in plasma with density low enough for laser light to propagate (underdense plasma) include the self-generated plasma cavity or 'bubble' produced in laser-driven wakefield acceleration [1] and plasma channels [2]. These structures are formed principally by the ponderomotive force induced by the propagating laser pulse, which expels electrons from the regions of high laser intensity, and by self-generated fields induced by the current displacement [3]. Shaping the spatial-intensity profile of a laser focus enables control over the collective electron motion and thereby the properties of the beams of high energy particles and radiation produced. In the case of wakefield acceleration, for example, the laser focal spot size is matched to the size of the plasma bubble as defined by the characteristic plasma oscillation frequency in order to optimize the acceleration [4]. For ultrashort pulses the degree of control on the intensity profile is typically limited to variation of the laser focal spot size by changing the F-number of the focusing optic or by using a deformable mirror to control the laser wavefront.

In the case of solid targets used for ion acceleration [5, 6] and high harmonic generation [7, 8], the laser light can propagate only to the region of the critical density at which the plasma frequency is equal to the laser light frequency. At the peak laser intensities achievable at present, plasma electrons oscillate at relativistic velocities such that an ultrathin foil undergoing expansion becomes relativistically transparent to the laser pulse [9–15]. Transparency can also be achieved if the electron layer is compressed to a thickness less than the plasma skin depth [16, 17]. The onset of transparency has been shown to affect the rising edge profile, duration and polarization of intense laser pulses [18–21] and the effect is important in driving new ion acceleration [22, 23] and radiation production [24–27] mechanisms. For the first time, we demonstrate that the intense laser light transmitted in ultrathin foil targets undergoing transparency is subject to the fun-

damental optical process of diffraction produced by a self-generated circular 'relativistic plasma aperture' and that the resulting near-field diffraction pattern defines the collective plasma dynamics. It is shown, via particle-in-cell (PIC) simulations and experiment, that this determines the spatial-intensity distribution of the beam of relativistic electrons accelerated, thus providing fundamental new understanding of current structure formation in the relativistic induced transparency (RIT) regime of laser-plasma interactions. We demonstrate control of the electron distribution by variation of the laser polarization to induce dynamic diffraction patterns.

NEAR-FIELD DIFFRACTION DURING RELATIVISTIC INDUCED TRANSPARENCY

The interference of waves which encounter a pinhole (or other obstacle) that is comparable in size to the wavelength gives rise to diffraction phenomenon according to the Huygens-Fresnel principle [28, 29]. In the case of a thin foil target undergoing RIT, a region of the target near the peak of the focused intensity becomes relativistically underdense to the laser light. In this region $n_e < n_c'$, where n_e is the plasma electron density and $n_c' = \gamma m_e \epsilon_0 \omega_L^2 / e^2$ is the relativistically corrected critical plasma density (γ is the Lorentz factor, m_e is the electron rest mass, ϵ_0 is the vacuum permittivity, ω_L is the angular laser frequency and e is the electron charge). The diameter of this circular region, shown schematically in Fig. 1a for a Gaussian laser pulse, depends on the intensity profile of the focal spot and the plasma expansion characteristics. It will typically be of the order of the full width at half maximum (FWHM) of the laser focus and therefore ~2-3 times the laser wavelength for a tightly focused (near diffraction limited) beam. Thus, after formation of this aperture on the pulse rising edge, the conditions are ideal for strong diffraction of the remainder of the laser pulse propagating through it.

We begin by considering the near-field diffraction pattern for the idealized case of a fixed aperture, i.e. without plasma evolution effects. Figure 1b shows 3D PIC simulation results in which a laser pulse with focal spot diameter of 3 μm (FWHM) is passed through a fixed 3 μm diameter circular aperture. The intensity distribution patterns in the Y-Z plane at three example X positions are shown in Fig. 1c. The near-field pattern (i.e. at small X) is observed to vary strongly with position from an analogous even-IG_{20} mode (Ince-Gaussian mode with ellipticity 0.1) at X = 0.4 μm to the odd-IG_{11} mode at X =

1.2 μm. The pattern diffracts into an even-IG_{00} mode in the far-field. The distribution is fully described by a vectorial analysis using Hertz Vector Diffraction Theory (HVDT) [30], as shown in Fig. 1d.

Next we replace the fixed aperture target with a uniform thin foil (i.e. initially without aperture) and investigate the laser-generated 'relativistic plasma aperture', the effect this has on the propagating laser light and in turn how the evolving laser spatial profile influences the beam of fast electrons accelerated forward. This is investigated using full 3D PIC simulations for the same laser pulse and target parameters as the experiment discussed below.

Figure 2a-d shows an example simulation result for the laser intensity and electron density just after RIT occurs. The laser light is linearly-polarized, along the Y-axis. Interference between laser light which is reflected from the target before RIT occurs and the remaining incoming laser light results in a standing wave distribution with local nodes and anti-nodes at the target front side (X<0). Despite local deformation of the target due to laser radiation pressure, during RIT the remainder of the laser pulse diffracts as it passes through the evolving plasma aperture. The resulting diffraction pattern at the target rear is very similar, in both the near and far fields, to that shown in Fig. 1. Furthermore, the simulation clearly shows that the accelerated electrons respond to the diffracted laser intensity distribution. In Fig. 2c, at the X position at which the electron density is highest on axis (X$\sim$1 μm), the laser profile has a double diffraction lobe distribution orientated perpendicular to the polarization direction, similar to the distribution shown in Fig. 1d, and an Airy disk distribution in the far field (X>4 μm), again similar to the far-field pattern in Fig. 1d. The electrons in the region of the double diffraction lobe are subject to a transverse ponderomotive force in the plane of the target, as shown by the hollow black arrows (from field mapping) in Fig. 2d. This drives the electrons into a double lobe distribution, perpendicular to the laser polarization direction. A smaller number of electrons are also trapped on-axis between the opposing ponderomotive forces of similar magnitude produced by the two laser diffraction nodes.

POLARIZATION SENSITIVITY

Given that diffraction in the near-field is sensitive to laser polarization, we next consider the extent to which the electron beam spatial distribution can be controlled by changing the polarization. The results in Fig. 2a-d are for linearly polarized pulses. Corresponding simulation results are presented for elliptical and circular polarization in Fig. 2e-g and Fig. 2h-j, respectively. The results are explained with reference to model calculations of the angular velocity of the polarization vector and magnitude of the electric field as shown in Fig. 2k-m for one laser period. In the linear polarization case the laser electric field flips between the two lobes over each half-laser period, producing the angular asymmetry in the ponderomotive force discussed above. With circularly polarized light, because the phase difference is $\pi/2$, the field components produce a dynamic intensity profile which makes a complete rotation at constant angular velocity around the laser propagation axis once per laser period. The instantaneous radial ponderomotive force is asymmetric, as shown in Fig. 2j, but when averaged over a laser period (or more) a ring-like electron distribution centred on the laser propagation axis is produced. The elliptical polarization ($\pi/4$ ellipticity) case exhibits elements of both types of behaviour. The polarization vector rotates, but with an angular velocity which varies over the laser period. The magnitude of the laser electric field is highest during the part of the laser period where the polarization vector rotates slowest, as seen when comparing the red phases of the curves in Fig. 2k-m. The plasma electrons respond to the angular variation in the radial ponderomotive force to produce a double lobe orientated perpendicular to the 'average' polarization axis (the red parts of the circle in Fig. 2g correspond to the red phases of the curves in Fig. 2k-m).

We note that the use of circularly polarized light results in significantly less electron heating and expansion and consequently more radiation-pressure-driven target deformation. RIT therefore occurs later in the interaction, producing a smaller aperture compared to the linear and elliptical cases.

The rotating laser diffraction structure instigates an in-phase rotation of a structure in the plasma electron density as shown in the time-resolved results in Fig. 3. The structure continues to rotate after the laser pulse has decayed, at ~120 fs, resulting in a two-component electron distribution: a main high energy component rotating with a small

radius of curvature about the propagation axis and a lower density of electrons which 'escape' from the rotating structure to larger radii, as shown in Fig. 3c.

The behaviour predicted in these simulations was tested experimentally using the Gemini laser [31], which delivers light with a central wavelength of 800 nm in pulses with 40 fs FWHM duration. The peak laser intensity for these measurements was 6×10^{20} Wcm^{-2} and the targets were 10 nm-thick Al. Figure 4 compares example time-integrated measurements of the electron beam measured in the Y-Z plane with the 3D EPOCH simulation results integrated over 5 laser cycles at the end of the pulse, for all three polarization cases. As the measurements are made 3 cm downstream from the target, the comparison is made in terms of electron angular deflection (as sampled at X=6 μm in the simulations). From the discussion above, the circular polarized case may be expected to produce an electron density ring due to the constant rotational velocity and electric field as shown in Fig. 2k-m. However, the simulations show that in fact there is a slight distortion in the polarization induced by the evolving plasma aperture, resulting in a ring-like distribution with localized maxima.

The experiment results verify the behaviour observed in the simulations for all three polarization cases, as shown in Fig. 4. The measured double-lobe electron density feature matches the simulation predictions in terms of the angular separation of the lobes and their orientation with respect to the polarization axes for both the linear and elliptical cases. The larger measured angular width of the lobes may result from space-charge spreading of the beam as it propagates downstream towards the detector. The measurements for circularly-polarized light reproduce both the small-radius central ring with local maxima (labelled 1) and the lower density distributions at larger radii (labelled 2) in Fig. 4c for electrons with energy greater than 3.5 MeV. The corresponding circular density profile for electrons with energies above 17 MeV is also reproduced experimentally, as shown in Fig. 4g.

We note that a double lobe electron density structure was observed in 3D simulations of ion acceleration in relativistically transparent thin foils by Yin *et al* [32], using linearly polarized laser light. In the analytical theory presented in that paper, the asymmetric double lobe effect is attributed to the plasma response to the radially symmetric laser intensity profile, and specifically to the combination of oscillatory and nonoscillatory electron momentum components in the plane perpendicular to the laser propagation

direction. We have previously reported an experimental observation of a similar double lobe structure, but again only for linearly polarized light [33]. By investigating the sensitivity of the electron distribution to the drive laser polarization, numerically and experimentally, the present study reveals that the underpinning physics giving rise to the lobe features arises from diffraction. This is further confirmed by simulations discussed below in which the relativistic plasma aperture diameter is varied.

ELECTRON SPATIAL PROFILE DEPENDENCE ON APERTURE SIZE

The relativistic plasma aperture diameter is defined by the condition $n_e < n_c'$ and increases with peak laser intensity for a given target material and thickness. Figure 5a-c and d-f shows p-polarization simulation results with the laser focus diameter (FWHM) equal to 1.5 μm and 6 μm, respectively. These results are directly comparable to the 3 μm case in Fig. 2a-d (the peak laser intensity and duration and target parameters are the same). The smaller aperture case results in a single laser diffraction node, stretched in the polarization direction (Y-axis), which ponderomotively expels electrons preferentially in both directions in Z, producing a double lobe electron density distribution. Unlike the 3 μm case, because a single laser node is produced on-axis there isn't a secondary low density axial electron population produced. With increasing aperture size the number of maxima in the near-field diffraction in the vicinity of the electrons increases. These take the form of intense laser 'stripes' orientated along the polarization direction, as shown in Fig. 5e. As clearly shown in Fig. 5f, the electrons are deflected to form a similarly striped pattern, interleaved with the laser stripes. The periodicity of this grating-like structure is 1.2 μm. Evolving structures of this type may find application in driving secondary radiation sources.

RESULTANT MAGNETIC FIELD STRUCTURES AND ANALOGOUS SYSTEMS

Our results provide the first demonstration that intense laser light is strongly diffracted in thin foils undergoing RIT and that the plasma electrons collectively respond to the resulting near-field diffraction pattern. It is shown that through suitable choice of laser drive parameters the spatial-intensity distribution of a high current beam of relativistic

electrons can be modified and that rotational, time-dependant structures can be induced. This opens up a new direction in spatial and temporal control of electron motion in dense plasma and by extension the evolution of the high fields used to accelerate charged particles and to produce high energy radiation.

These dynamic diffraction effects can give rise to interesting and potentially useful magnetic field structures. By observing the resultant magnetic field from the circularly polarized laser-diffraction and collective plasma behaviour, it can be seen that the magnitude of the magnetic field becomes helical in structure, tightly precessing at a radius close to that of the plasma aperture (0.75 μm), as shown in Fig. 6a. When compared to the magnetic field generated by a lower intensity (but otherwise identical) circularly polarized laser, propagating through a comparable fixed circular aperture of 0.75 μm radius (i.e. no plasma; Fig. 6b), it is clear that the diffraction effects play a key role in the formation of such a magnetic field structure. This magnetic field is shown in both cases 30 fs after the peak laser intensity has propagated through the aperture. The laser pulse propagating through the fixed aperture produces a magnetic field which is strongest close to the aperture, reducing as the beam expands. By contrast, in the relativistic plasma aperture case the magnetic field is strong over a longer range and is more helical, suggesting that the field is modified by the induced plasma current structure. The underlying physics of the collective plasma effects on the magnetic field will be the subject of future investigation.

The current and field structures produced in this way could be used to generate laboratory analogues of astrophysical phenomena. Similar magnetic field structures have been detected in jets originating from active galactic nuclei, such as 3C 273 [34]. Such structures are commonly identified as being generated from the rotation of the accretion disk, whilst the analogous structures seen here arise from the rotation of the diffraction pattern. Further similarities to these jets can be observed in that the highest momentum component of the accelerated electrons occur along the central laser axis. Surrounding this region, the electron momentum reduces, as seen in Fig. 6, resulting in an electron beam with properties similar to that of the spine-sheath jet morphology [35].

In another example, similar helical magnetic fields as those in Fig. 6 have been artificially generated using field coils within centimetre-scale plasma and shown to excite electron whistler modes [36]. It is therefore possible that within the circularly polarized

laser-plasma interaction that similar whistler modes are being generated.

The present work reveals a new phenomenon in relativistic plasma optics. It provides new insight into fundamental aspects of laser-matter interactions in the relativistic intensity regime and identifies the emergence of optically controlled dynamic current structures in dense plasma. This stimulates the exploration of new avenues in laboratory astrophysics and in novel radiation and particle source development.

METHODS

Experiment

The experiment results were obtained using the Gemini [31] Ti:sapphire laser at Rutherford Appleton Laboratory in the UK. The central wavelength is optimized at 800 nm and the pulse duration was 40 fs (FWHM). The laser beam was focused along target normal onto the front surface of 10 nm-thick aluminium foils, using an off-axis $f/2$ parabola, to a focal spot diameter of 3 μm (FWHM). The laser pulse energy was 2 J, giving a calculated peak intensity of 6×10^{20} Wcm^{-2}. A double plasma mirror configuration was used to enhance the intensity contrast to $\sim10^{11}$ and $\sim10^{8}$, at 1 ns and 5 ps, respectively, prior to the peak of the pulse. A deformable mirror was used prior to the focusing parabola to ensure a high quality focal spot on target. Thin mica wave plates were used to switch between linear ($\Delta\theta = 0$), elliptical ($\Delta\theta = \pi/4$) and circular ($\Delta\theta = \pi/2$) polarization, where $\Delta\theta$ is the phase difference between the two orthogonal components of the laser beam. The 2D spatial-intensity distribution of the electron beam was measured 3 cm downstream from the target using passive stacked layers of Fujifilm imaging plate, interleaved with iron filters to provide energy filtering. The filtering before the first layer is sufficient to prevent the detection of any protons or heavier ions produced.

Analytical modelling

The analytical modelling of the diffraction pattern produced by a laser pulse passing through a circular aperture, as shown in Fig. 1, was performed using Hertz Vector Diffraction Theory (HVDT) [30]. With this vectorial model, values for the electromagnetic field can be obtained not only in the plane of the aperture but also downstream.

The near-field diffraction pattern, in the region of maximum interaction between the laser and the plasma electrons, is of particular interest here. Although other analytical models like the scalar Rayleigh-Sommerfeld [37] or Fresnel-Kirchhoff [38] models can be used to study diffraction induced by an aperture, they work in the limit that the aperture radius is much bigger than the laser wavelength, that the electric field in the plane of the aperture is known and involve a scalar treatment of the diffracted light. We use the HVDT model to avoid these limitations.

The analytical results reported in Fig. 2k-m were obtained by solving the following equations which describe the two orthogonal electric field components for the different polarizations considered. The orthogonal electric field components are $\vec{E_y} = E_{0y} \cdot sin(\phi)\vec{y}$ and $\vec{E_z} = E_{0z} \cdot sin(\phi - \Delta\theta)\vec{z}$, where $\Delta\theta$ is the phase difference. For linear polarization $\Delta\theta = 0$ and $E_{0z} = 0$; for elliptical polarization $\Delta\theta = \pi/4$ and $E_{0y} = E_{0z}$; and for circular polarization $\Delta\theta = \pi/2$ and $E_{0y} = E_{0z}$. The angle with respect to the +Y axis is $\theta_{\vec{E_y}\vec{E_z}} = tan^{-1}\left(\vec{E_z}/\vec{E_y}\right)$ and the rotational angular velocity with respect to the +Y axis is $\omega_R = {}^{d\theta_{\vec{E_y}\vec{E_z}}}/dt$. The magnitude of the total electric field is $\| E_T(\vec{E_y}, \vec{E_z}) \| = \sqrt{\vec{E_y}^{\,2} + \vec{E_z}^{\,2}}$.

Simulations

The simulations were performed using the fully relativistic 3D EPOCH particle-in-cell (PIC) code [39]. The simulation space is defined as a 20 μm × 20 μm × 20 μm box with 1000 × 720 × 720 computational mesh cells. The laser wavelength is 800 nm. The pulse has a Gaussian temporal profile with 40 fs FWHM width, focused to a Gaussian intensity distribution of 3 μm FWHM. The peak laser intensity is $6{\times}10^{20}$ Wcm^{-2}. Simulations are performed with the laser pulse polarized linearly (p-polarization), elliptically (ellipticity of $\pi/4$) or circularly. The simulations are run for a total duration of 200 fs to ensure full propagation of the laser pulse through the simulation space. The target is a fully ionized 10 nm-thick Al^{13+} slab with 6 nm-thick C^{6+} and H^+ mixed contamination layers (assumed to be a hydrocarbon with the form C_2H_6) on the front and rear surfaces. In order to resolve the physics within such an ultra-thin target, it is necessary to pre-expand the target and contamination layers with a 245 nm FWHM Gaussian profile, giving peak densities of $\sim 1.3 n_c$ Al^{13+}, $\sim 1.3 n_c$ H^+ and $\sim 0.4 n_c$ C^{6+}, where n_c is the critical plasma density. The density of the electrons was initialized to neutralize the ions and the initial

electron temperature was set at 100 keV. Initially there were ~22 simulation particles per cell per species (total of 3.11×10^9 simulation particles). The code assumed no binary collisions.

REFERENCES

[1] Pukhov, A. & Meyer-ter-Vehn, J. Laser wake field acceleration: the highly non-linear broken-wave regime. *Appl. Phys. B* **74,** 355-361 (2002)

[2] Pukhov, A. & Meyer-ter-Vehn, J. Relativistic magnetic self-channeling of light in near-critical plasma: three-dimensional particle-in-cell simulation. *Phys. Rev. Lett.* **76,** 3975 (1996)

[3] Kaluza M.C. *et al.* Measurement of magnetic-field Structures in a laser-wakefield accelerator. *Phys. Rev. Lett.* **105,** 115002 (2010)

[4] Thomas A.G.R. *et al.* Effect of laser-focusing conditions on propagation and monoenergetic electron production in laser-wakefield accelerators. *Phys. Rev. Lett.* **98,** 095004 (2007)

[5] Daido H. *et al.* Review of laser-driven ion sources and their applications. *Rep. Prog. Phys.* **75,** 056401 (2012)

[6] Macchi A. *et al.* Ion acceleration by superintense laser-plasma interaction. *Rev. Mod. Phys.* **85,** 751 (2013)

[7] Ganeev R.A. High-order harmonic generation in a laser plasma: a review of recent achievements. *J. Phys. B: At. Mol. Opt. Phys* **40,** R213 (2007)

[8] Dromey B. *et al.* High harmonic generation in the relativistic limit. *Nature Phys.* **2,** 456-459 (2006)

[9] Kaw P. and Dawson J. Relativistic nonlinear propagation of laser beams in cold overdense plasmas. *Phys. Fluids* **13,** 472 (1970)

[10] Guerin S. *et al.* Propagation of ultraintense laser pulses through overdense plasma layers. *Phys. Plasmas* **3,** 2693 (1996)

[11] Fuchs J. *et al.* Transmission through highly overdense plasma slabs with a subpicosecond relativistic laser pulse. *Phys. Rev. Lett.* **80,** 2326 (1998)

[12] Cattani F. *et al.* Threshold of induced transparency in the relativistic interaction of an electromagnetic wave with overdense plasmas. *Phys. Rev. E.* **1234,** (2000)

[13] Tushentsov M. *et al.* Electromagnetic energy penetration in the self-induced transparency regime of relativistic laser-plasma interactions. *Phys. Rev Lett.* **87,** 275002 (2001)

[14] Willingale L. *et al.* Characterization of high-intensity laser propagation in the relativistic transparent regime through measurements of energetic proton beams. *Phys. Rev. Lett.* **102,** 125002 (2009)

[15] Eremin V.I. *et al.* Relativistic self-induced transparency effect during ultraintense laser interaction with overdense plasmas: why it occurs and its use for ultrashort electron bunch generation. *Phys. Plasmas* **17,** 043102 (2010)

[16] Vshivkov V.A. *et al.* Nonlinear electrodynamics of the interaction of ultra-intense laser pulses with a thin foil. *Phys. Plasmas* **5,** 2727 (1998)

[17] Yu W. *et al.* Model for transmission of ultrastrong laser pulses through thin foil targets. *Phys. Rev. E* **59,** 3583 (1999)

[18] Reed S.A. *et al.* Relativistic plasma shutter for ultraintense laser pulses. *Appl. Phys. Lett.* **94,** 201117 (2009)

[19] Wang H.Y. *et al.* Laser shaping of relativistic intense, short Gaussian pulse by a plasma lens. *Phys. Rev. Lett.* **107,** 265002 (2011)

[20] Palaniyappan S. *et al.* Dynamics of relativistic transparency and optical shuttering in expanding overdense plasmas. *Nature Phys.* **8,** 11 (2012)

[21] Stark. D.J. *et al.* Relativistic plasma polarizer: impact of temperature anisotropy on relativistic transparency. *Phys. Rev. Lett.* **115,** 025002 (2015)

[22] Henig. A. *et al.* Enhanced laser-driven ion acceleration in the relativistic transparency regime. *Phys. Rev. Lett.* **103,** 045002 (2009)

[23] Macchi A. *et al.* "Light Sail" acceleration reexamined. *Phys. Rev. Lett.* **103,** 085003 (2009)

[24] Dromey B. *et al.* Coherent synchrotron emission from electron nanobunches formed in relativistic laser-plasma interactions. *Nature Phys.* **8,** 11 (2012)

[25] Dromey B. *et al.* Coherent synchrotron emission in transmission from ultrathin relativistic laser pasmas. *New J. Phys.* **15,** 015025 (2013)

[26] Kiefer D. *et al.* Relativistic electron mirrors from nanoscale foils for coherent frequency upshift to the extreme ultraviolet. *Nat. Commun.* **4,** 1763 (2013)

[27] Yeung M. *et al.* Dependence of laser-driven coherent synchrotron emission efficiency on pulse ellipticity and implications for polarization gating. *Phys. Rev. Let.* **112,** 123902 (2014)

[28] Fresnel A. Memoire sur la Diffraction de la Lumiere *Ann. Chim et Phys.* **1,** 129 (1816)

[29] Stratton, J.A. & Chu, L.J. Diffraction theory of electromagnetic waves. *Phys. Rev.* **56,** 99–107 (1939)

[30] Guha, S. & Gillen, G. Description of light propagation through a circular aperture using nonparaxial vector diffraction theory. *Opt. Express* **13,** 1424-1447 (2005)

[31] Hooker C.J. *et al.* The Astra Gemini project - A dual-beam petawatt Ti:Sapphire laser system. *J. Phys. IV France* **133,** 673-677 (2006)

[32] Yin, L. *et al.* Three-Dimensional dynamics of breakout afterburner ion acceleration using high-contrast short-pulse laser and nanoscale targets. *Phys. Rev. Lett.* **107,** 045003 (2011)

[33] Gray, R.J. *et al.* Azimuthal asymmetry in collective electron dynamics in relativistically transparent laser-foil interactions. *New J. Phys.* **16,** 093027 (2014)

[34] Asada K. *et al.* A helical magnetic field in the jet of 3C 273. *Publ. Astron. Soc. Japan* **54,**(3) L39-L43 (2002)

[35] Ghisellini G. *et al.* Structured jets in TeV BL Lac objects and radiogalaxies. *Astron. Astrophy.* **432,** 401-410 (2005)

[36] Urrutia J. M. and Stenzel R. L. Magnetic antenna excitation of whistler modes. I. basic properties. *Phys. Plasmas* **21,** 122107 (2014)

[37] Rayleigh, J.W. On the passage of waves through apertures in Plane screens, and allied problems. *Philos. Mag.* **43,** 259-272 (1897)

[38] Kirchhoff, G.R. Zur theorie der lichtstrahlen. *Ann. Phys.* **254,** 663-695 (1883)

[39] Brady C.S. and Arber T.D. An ion acceleration mechanism in laser illuminated targets with internal electron density structure. *Plasma Phys. Control. Fusion* **53,** 015001 (2001)

ACKNOWLEDGMENTS

We thank the Gemini team at the Central Laser Facility of the Rutherford Appleton Laboratory for their support during the experiment; in particular, N. Booth and D. Symes. We acknowledge the use of the ARCHIE-WeST and ARCHER high performance computers. This work is supported by EPSRC (grants: EP/J003832/1, EP/L001357/1, EP/K022415/1 and EP/L000237/1), STFC (grant number ST/K502340/1) and the US Air Force Office of Scientific Research (grant: FA8655-13-1-3008). EPOCH was devel-

oped under EPSRC grant EP/G054940/1.

AUTHOR CONTRIBUTIONS

B.G.-I., R.J.G., M.K. and P.M. conceived the experiment. R.J.G., R.J.D., B.G.-I., R.W., J.M., N.M.H.B., S.H., J.S.G. and P.M. executed the experiment and B.G.-I. and R.J.G. performed the analysis of the experimental data. M.K. and B.G.-I. performed the simulations and analysis of the simulation results, with contributions from R.C.. P.M. provided overall supervision of the work, with contributions from D.N. and M.B.. The manuscript was prepared by P.M., B.G.-I., M.K. and R.J.G. with contributions from all authors.

ADDITIONAL INFORMATION

Data associated with research published in this paper can be accessed by contacting the corresponding author.

COMPETING FINANCIAL INTERESTS

The authors declare no competing financial interests.

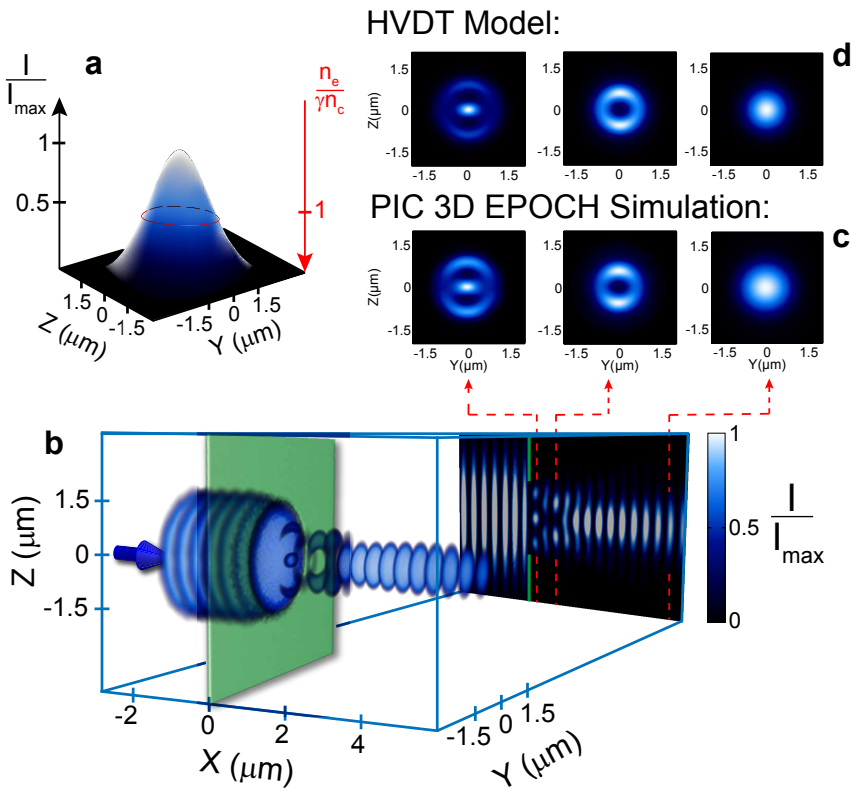

Figure 1: **Intensity diffraction pattern induced by a fixed aperture.** **a**, Schematic showing the Gaussian spatial-intensity distribution of an ultraintense laser pulse with diameter (FWHM) equal to 3 μm. For the case of near-critical, dense plasma, relativistic induced transparency occurs at intensities above those bounded by the ring corresponding to the threshold condition ($n_c' = n_e$), enabling this portion of the laser pulse to be transmitted; **b-c**, Simulation output showing the spatial-intensity variation of the diffraction pattern of a laser pulse with 3 μm (FWHM) diameter passing through a fixed 3 μm-diameter aperture: **b**, 3D profile and 2D (X-Z) cut-away in the Y=0 plane; **c**, 2D profile in the plane of the target at X=0.4 μm, X=1.2 μm and X=5.2 μm, exhibiting mode structures; **d**, Calculated diffraction patterns at the same three positions using Hertz vector diffraction theory.

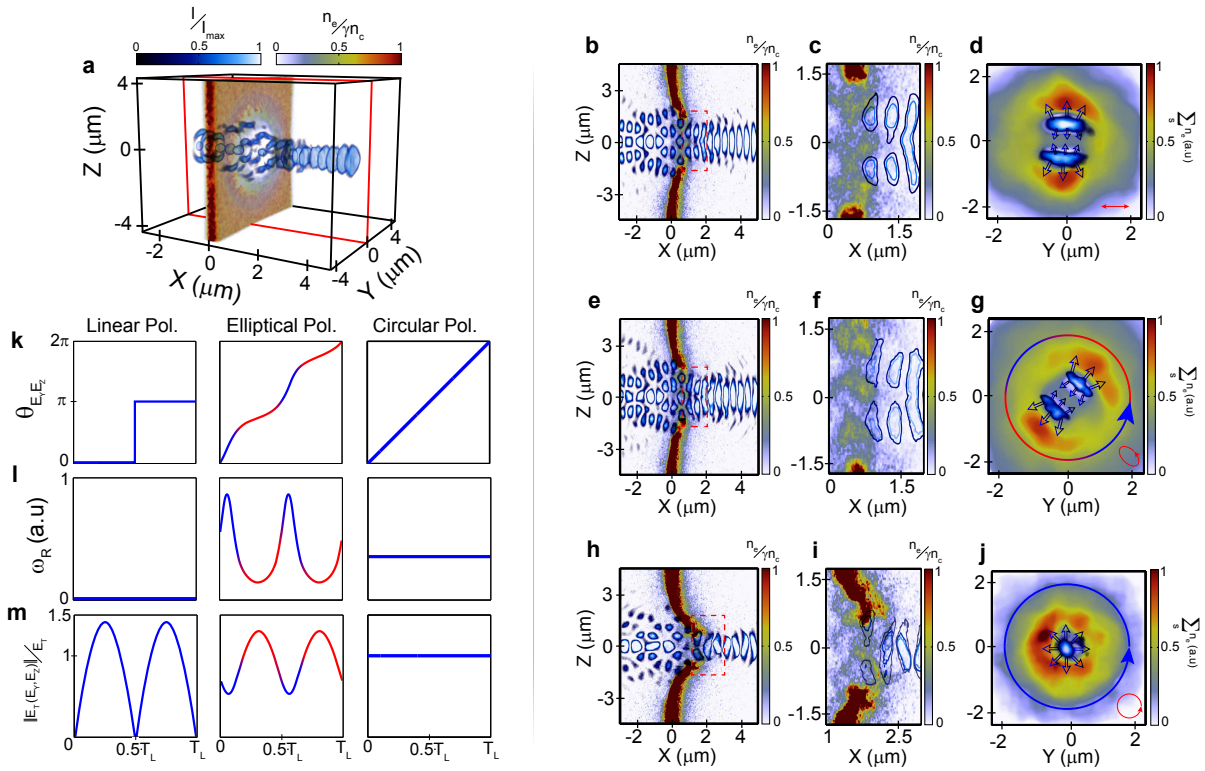

Figure 2: **3D-PIC simulations of laser diffraction and plasma electron density produced by the relativistic plasma aperture.** **a**, Example simulation result showing the laser intensity, I, pattern overlapped with the plasma electron density normalized to n_c', at 20 fs after RIT occurs. The diffraction pattern is very similar to the fixed aperture case without plasma shown in Fig. 1. The laser is linearly polarized in the Y-axis in both cases. **b**, 2D (X-Z) cut-away in the Y=0 plane (red plane highlighted in **a**) showing the diffraction pattern and electron density. **c**, Same showing the region of interest bounded by the dashed rectangle in **b**. The laser is delineated here as a contour to show that the electron distribution is modulated by the laser diffraction pattern. **d**, 2D (Y-Z) plane showing laser light intensity and electron density integrated over X=0.7 – 1.5 μm (corresponding to one laser wavelength in the region of the high density of electrons that are accelerated forward). The hollow black arrows illustrate the direction of the ponderomotive force arising from the gradients in laser intensity. **e-g**, Same for elliptically polarized laser light, with the X-Z plane corresponding to the projection of a 45° rotated plane around the laser propagation axis. **h-j**, Same for circularly polarized light. The red arrow inserts indicate the laser polarization. **k-m**, Model representation of: **k**, angle of the polarization vector with respect to the +Y axis; **l**, angular velocity of the polarization vector rotation with respect to the +Y axis; and **m**, magnitude of the laser electric field, for all three polarization cases over one laser period, T_L. The red 'phase' highlights the corresponding region in the rotation of the diffraction pattern shown in **g**.

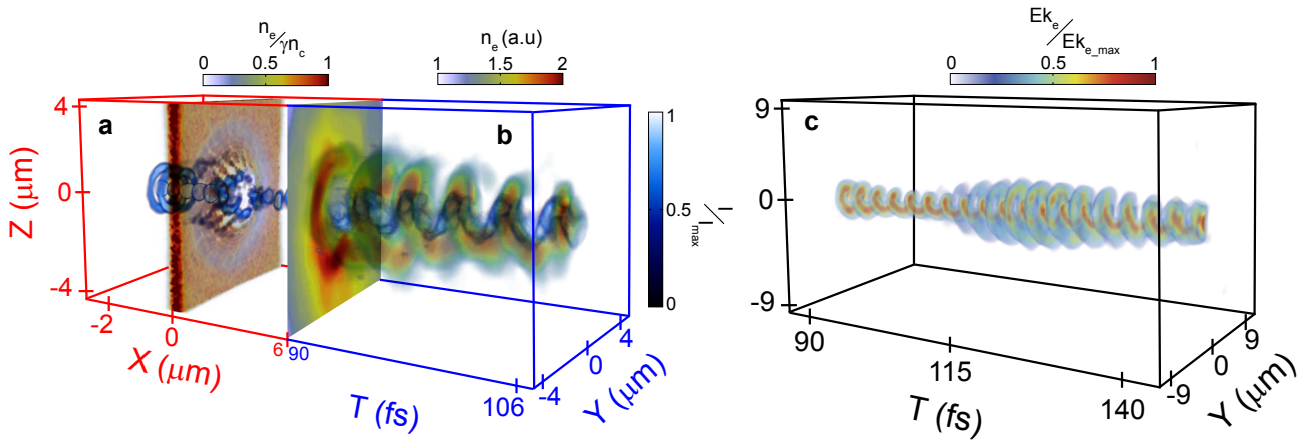

Figure 3: **3D PIC simulation results for circularly polarized light. a-b**, Combined plot showing **a**, the 3D laser intensity profile (up to X=6 μm) at 100 fs, and **b**, temporal evolution of the electron density distribution, overlaid with the laser intensity distribution, in the Y-Z plane at X=6 μm from 90 to 107 fs. **c**, Temporal evolution of the electron energy in the Y-Z plane at X=6 μm up to 145 fs. The laser diffraction lobe pattern rotates once per laser cycle driving an electron energy and density distribution which rotates in phase with it. The rotational velocity imparted on the electrons drives their rotation after the laser pulse has passed.

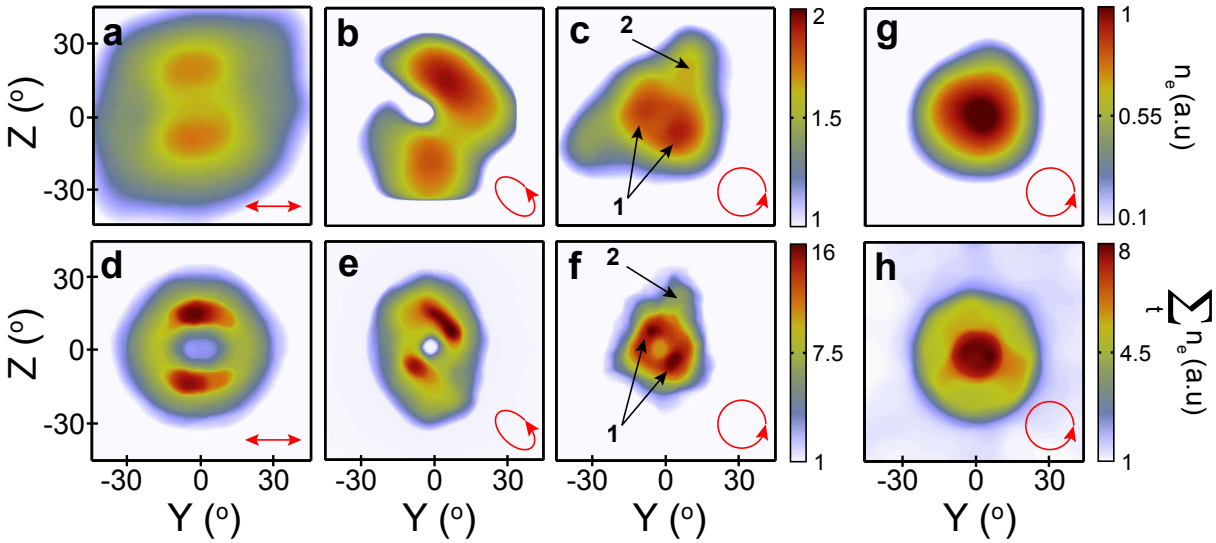

Figure 4: **Experiment and 3D PIC simulation results for the electron density distribution**. **a-c**, Electron density as measured using image plate for electrons with energy greater than 3.5 MeV, with linear, elliptical and circular polarized laser pulses, respectively. **d-f**, Simulated time-integrated electron density in the plane Y-Z at 6 μm downstream from the rear side of the target, corresponding to linear, elliptical and circular polarization, respectively. The electron energy distribution is integrated for 'low' energies (from 1-6 MeV). **g-h**, Corresponding experiment, **g**, and simulation, **h**, results for the circular polarization case for 'high' energies (above 17 MeV). The features labelled 1 and 2 in **c** and **f** are discussed in the main text.

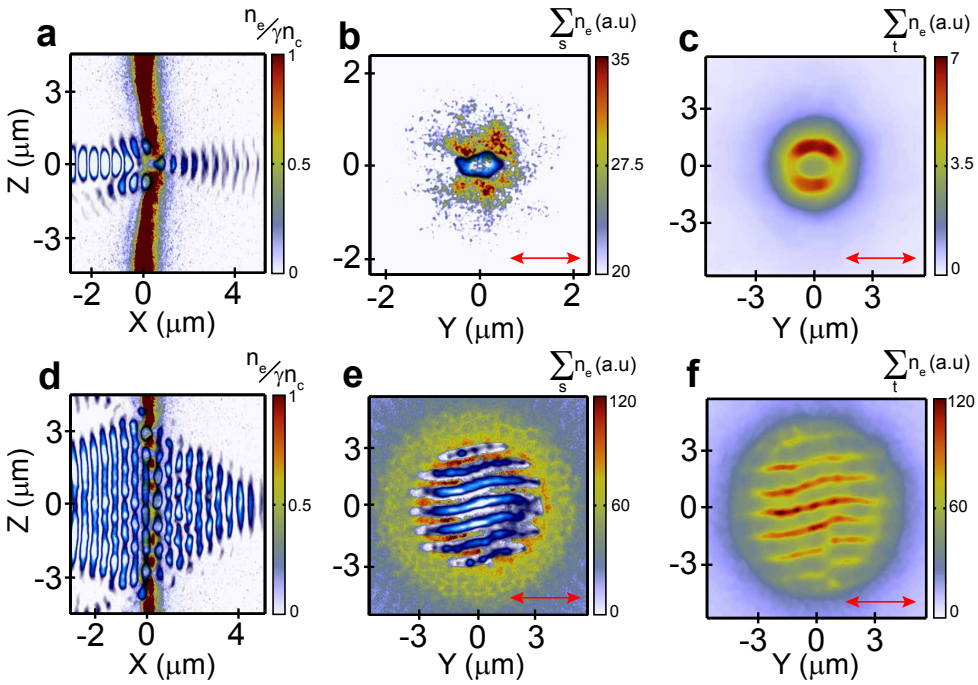

Figure 5: **3D EPOCH simulation with laser focal spot size equal to 1.5 μm and 6 μm**. **a**, Laser intensity and electron density in the X-Z plane at Y = 0, for a 1.5 μm (FWHM) focal spot. **b**, Y-Z plane with n_e/n_c' overlapped with the laser intensity profile (both spatially integrated over X = 0.7-1.5 μm). **c**, Time integrated electron density in the Y-Z plane at X=6 μm. **d-f**, Same as **a-c** but with a laser focal spot diameter equal to 6 μm (FWHM). In both cases the laser is linearly polarized in the Y-axis.

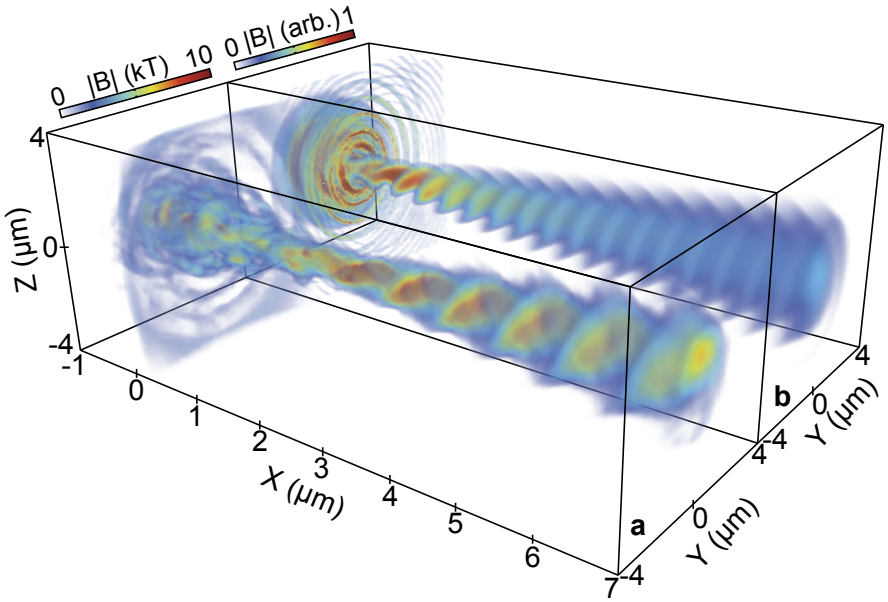

Figure 6: **Magnetic field structure driven by circularly polarized light**. **a**, Magnitude of the magnetic field driven by a circularly polarized laser pulse producing a relativistic plasma aperture in a 10 nm-thick Al target. A helical field structure is produced. **b**, Same for the case of a lower intensity laser pulse propagating through a fixed, predefined aperture of 0.75 μm radius, i.e. without plasma effects. The 3 μm (FWHM) laser focus is centred on [X,Y,Z]=[0,0,0] in both cases and the field is sampled 30 fs after the peak of the laser intensity. Diffraction induced by the aperture results in a helical field profile in both cases. The structure is modified by the presence of plasma in **a**.